THE ASTROPHYSICAL JOURNAL, 468:86–96, 1996 September 1

BROAD BAND X-RAY TELESCOPE OBSERVATIONS OF THE CLUSTERS OF GALAXIES ABELL 262 AND ABELL 496

MEREDITH MACKENZIE,[1,2] ERIC M. SCHLEGEL,[3,4,5] AND RICHARD MUSHOTZKY[6]

Received 1995 September 29; accepted 1996 March 22

ABSTRACT

The galaxy clusters A496 and A262 were observed by the Broad Band X-Ray Telescope (BBXRT) during the Astro-1 mission. A496 was observed for 2282 s; A262 was observed for 5547 s. Observations ranged from 2′ to 13′ off-axis. BBXRT had ~160 eV resolution at 6 keV and moderate spatial resolution. The A496 data reveal the cooling flow present in this cluster but are consistent with a constant abundance and column density. An unresolved iron line is present at 6.46 keV with an equivalent width of 600 eV; this line is consistent with Fe XXV. The A262 data are of limited value. The spectra are consistent with no cooling gradient, no abundance gradient, and no column density gradient across the cluster. We also assign an upper limit of 1 keV to the presence of an iron line.

Subject headings: cooling flows — galaxies: clusters: individual (Abell 262, Abell 496) — intergalactic medium — line: identification — X-rays: galaxies

1. INTRODUCTION

The X-ray emission from clusters of galaxies is consistent with optically thin thermal bremsstrahlung emission from hot gas (e.g., Sarazin 1988; Mushotzky 1994; Fabian 1994) confined by the gravitational potential well of the cluster. A critical temperature in the cooling function exists at $\sim 2 \times 10^7$ K (~1.7 keV): above this temperature, thermal bremsstrahlung continuum emission dominates the spectra, while below this temperature, line cooling dominates. With the detection of the iron line from the Perseus cluster (Mitchell et al. 1976) and the Coma and Virgo clusters (Serlemitsos et al. 1977), interest increased in understanding the details of the X-ray emission as probes of the physics of clusters and their intracluster gas. Heavy elements, particularly iron, dominate the emission. The origin of these elements is not understood, but a reasonable model is the injection of nucleosynthesis products into the intracluster gas by supernovae and the stellar winds of massive stars.

The details of the X-ray emission must be investigated with high–spatial and spectral resolution instruments. High–spectral resolution observations provide information on gas temperatures, element abundances, and absorption along the line of sight. High spatial resolution provides information or limits on substructure in the X-ray emission, possible correlations of the optical galaxies with any X-ray substructure, and the cluster X-ray emission profile. White et al. (1991), for example, found excess absorption (above the Galactic contribution) in several clusters; the implication is that a considerable mass ($\sim 10^{12}\ M_\odot$) of cold material is present. White et al. (1994) found, using combined *Einstein* solid-state spectrometer (SSS) and *Ginga* large area counter (LAC) data, that two-temperature fits were necessary to fit the data. They also showed that fits to the data required elevated column densities and abundances.

The flight of the Broad Band X-Ray Telescope (BBXRT), carried aloft by the Space Shuttle during the Astro-1 flight in 1990 December, provided an opportunity to study clusters with broadband, moderate resolution spectra. This paper presents the BBXRT data on the clusters A496 and A262. X-ray emission was discovered from both clusters by *Uhuru* (Forman et al. 1978) and imaged with the *Einstein* IPC (Stewart et al. 1984). The temperature of A496, based upon the *EXOSAT* medium-energy (ME) spectrum, is $4.8^{+0.9}_{-0.8}$ keV and yields a 2–10 keV luminosity of 2.5×10^{44} ergs s^{-1} (Edge et al. 1990). Nulsen et al. (1982) derived a mass accretion rate of $\sim 200\ M_\odot\ \mathrm{yr}^{-1}$ from *Einstein* data. For A262, the temperature is 2.4 ± 0.3 keV and the 2–10 keV luminosity is 2.7×10^{43} ergs s^{-1} (Edge et al. 1990).

The plan of the paper is as follows. Section 2 reviews the BBXRT instrument and describes the observations. Section 3 describes the spectral fitting that was done. Section 4 discusses the results.

2. OBSERVATIONS

The BBXRT flew on the eight-day Astro-1 Shuttle Mission in 1990 December. BBXRT was designed and built at GSFC (Serlemitsos et. al. 1992) and was the first X-ray telescope to operate over a broad spectral range (0.3–10 keV) with moderate energy resolution (~90 eV at 1 keV and ~160 eV at 6 keV). This spectral range overlaps with that of the *Advanced Satellite for Cosmology and Astrophysics* (*ASCA*) and so will provide cross-calibration capabilities on targets observed by both instruments. The BBXRT instrument consisted of two co-aligned telescopes of 3.8 m focal length, each with five lithium-doped silicon spectrometers arranged as in Figure 1 (to be described in greater detail). Some spatial resolution is provided by the individual pixels and is characterized by the pixel size. The mirrors are thin, nested, gold-coated aluminum foils, with an effective area of 150 cm^2 at 2 keV and 80 cm^2 at 7 keV for each telescope-detector combination. The overall field of view is 17′. The central pixel has a 4′.5 field of view and the pixels are separated by a mask 1′.5 across. The detector

---

[1] Summer Graduate Student Research Program.

[2] Astronomy Department, University of Maryland, College Park, MD 20742.

[3] Research Scientist, Universities Space Research Association.

[4] Code 660.2, NASA-GSFC.

[5] Current address: High-Energy Astrophysics Division, Harvard-Smithsonian Center for Astrophysics, 60 Garden Street, Cambridge, MA 02138.

[6] Code 662, NASA-GSFC, Greenbelt, MD 20771.

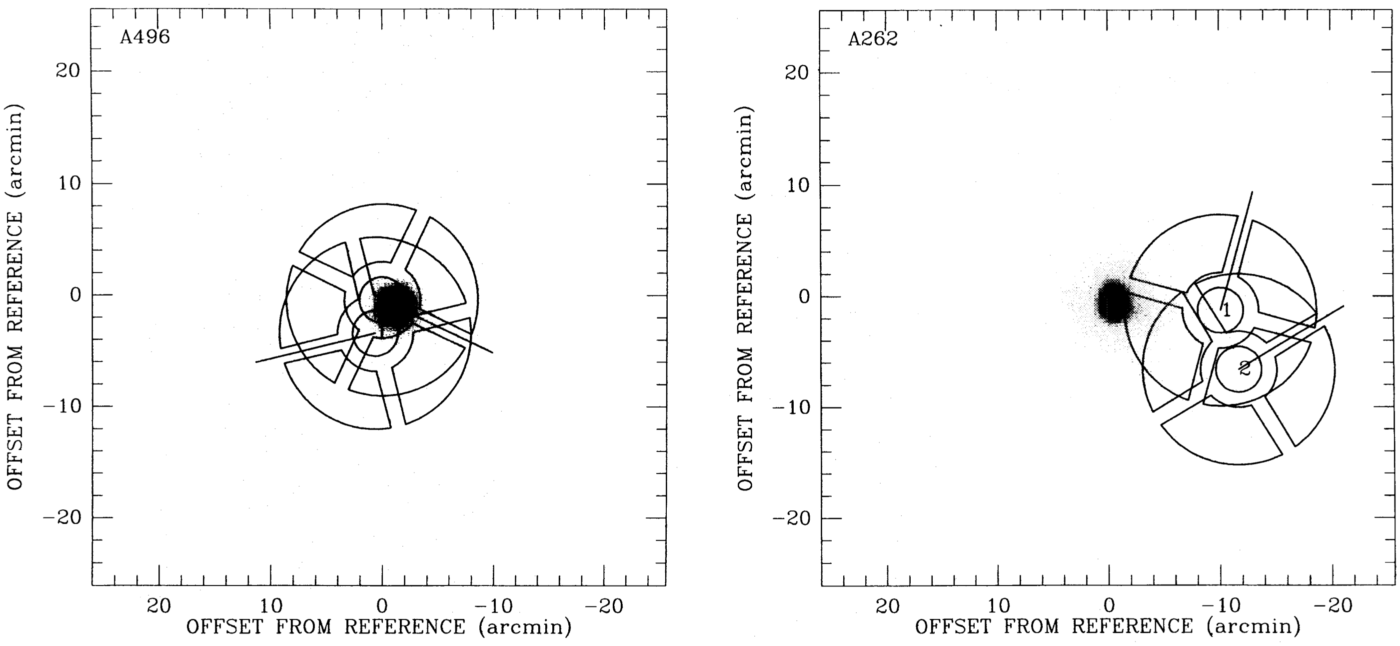

FIG. 1*a*

FIG. 1*b*

FIG. 1.—BBXRT pixel configuration overlaid on *Einstein* IPC images of each cluster. Only the pixels for telescope A are shown. The B telescope is offset slightly from the A telescope and is rotated 180° so that the A1 pixel overlaps the B3 pixel. The A1/A2 border is indicated by the tick mark originating at the central pixels. Two representative pointings (Table 1) for each cluster are shown. (*a*) A496, pointings 2 and 4; (*b*) A262, pointings 1 and 4.

backgrounds are low, with 0.02 counts s^{-1} in the central pixel and 0.1 counts s^{-1} in the outer pixels.

An aspect camera attached to BBXRT recorded aspect solutions of the telescope pointing as a function of time. Overlay plots were produced using an *Einstein* image of each cluster with the position of BBXRT taken from the aspect file projected onto the sky (Fig. 1). The pointings were, in general, sufficiently accurate that each pointing can been represented by a single aspect solution.

A496 was observed on days 2 and 3, and twice on day 5 of the Astro-1 mission (Table 1). The observation from day 2 and the first observation from day 5 were completely off-target. The remaining observations from days 3 and 5 totaled almost 3100 s. One pointing was nearly on-axis and the other only 4′ off-axis. Figure 1*a* shows two representative pointings of BBXRT in relation to the cluster. Most of these data were taken at night, with the nearest earth limb dark. There is a small portion of data taken during Shuttle day, but examination of the light curves indicate that background contamination is negligible. Data collected when the earth angle was less than 100° were filtered out of our observations. This amounted to less than 5% of the total integration time. All data were taken outside of the South Atlantic Anomaly, and other housekeeping parameters indicated no need for further filtering.

A262 was observed on days 5 and 7 of the Astro-1 mission for a total of over 5500 s (Table 1). All pointings were off-axis, so the signal was relatively weak, despite the

TABLE 1

LOG OF OBSERVATIONS

Observation	Off-Axis Angle (arcmin)	MET[a]	Usable Exposure	R.A. (hr)	Decl. (deg)	Aspect Solution[b]
			A496[c]			
1	>60	2-15:45	0	164	− 62	352
2	4	3-09:55	1789	67.87	− 13.41	28.7
3	44	5-17:13	0	67.85	− 12.63	251.0
4	2	5-17:25	493	67.85	− 13.36	250.5
			A262[c]			
1	9	7-08:27	2030	27.27	35.89	148.0
2	13	7-13:01	683	27.20	35.93	169.2
3	4	7-13:22	933	27.39	35.88	170.0
4	13	5-12:11	1901	27.24	35.81	193.8

[a] Mission elapsed time (MET), in which MET 0.0 (day 336.284039 of 1990) equals JD 2,448,227.784039.

[b] Aspect solution is the position on the sky of the center of the A0 pixel. An angle ϕ of zero indicates the A4 pixel is north of the central pixel on the sky. Positive values indicate clockwise rotation.

[c] Cluster coordinates (1950): A262: R.A. = $1^{\mathrm{h}}.83$, decl. = $+35^\circ.90$; A496: R.A. = $4^{\mathrm{h}}.52$, decl. = $-13^\circ.37$.

apparently long integration times. Figure 1*b* shows two representative pointings of BBXRT in relation to the cluster. Calibration problems due to airglow did not arise, since nearly all of the data were taken during Shuttle night. Observation 2 was collected during Shuttle day with the nearest earth limb dark, and the resulting variations in the light curve were negligible. Again, data with earth angles of less than 100° were filtered out, and all other housekeeping parameters indicated no additional filtering was necessary.

Internal background files were produced for each pixel following the procedure outlined by Weaver et al. (1995). This process involves scaling the internal background files to the anticoincidence rate, if necessary. The resulting file is then added to the diffuse nighttime X-ray background, which was observed throughout the mission. Both unscaled internal background files and diffuse background files were produced and are available from the BBXRT data archive. According to Weaver et al. (1995), the internal background reaches a lower threshold value for anticoincidence rates below 1000, and scales linearly with rates over 1000. Each observation had an overall rate less than 1000, so no scaling of the background files was necessary. When pixels were co-added for spectral fitting, their corresponding internal background files were also co-added.

3. SPECTRAL FITTING

3.1. *General Procedure*

Spectral fits were done by using the minimum χ^2 statistic option of the XSPEC (version 8.4) package. Pixels were co-added or fit simultaneously, as detailed below, with an absorbed Raymond-Smith thermal model. We want to preserve as much spatial information as possible to study any gradients in physical parameters that may exist, yet we also want to obtain the highest signal-to-noise spectrum possible for each cluster. Unfortunately, these two goals are somewhat incompatible given the relatively short pointings characteristic of the BBXRT data.

A spectrum was first obtained for each individual pixel and a best-fit model was produced for each. As the signal-to-noise ratio for a given spectrum is low, and because the spectral fits gave consistent temperatures in many of the pixels, some pixels could be added together to increase signal strength without any loss of effective spatial resolution. Pixels having gas temperatures consistent within the error bars were added together provided that their projected radial separations differed by less than 1′. We describe below our handling of pixels with different response matrices.

For all spectral fits, the redshift parameter in the Raymond-Smith model was fixed at the measured values of $z = 0.0164$ for A262 and $z = 0.0316$ for A496 (Sarazin 1988). In passing, we note that the Galactic column density $N_{\rm H}$ to each cluster is 4.9×10^{20} cm^{-2} for A262 and 4.5×10^{20} cm^{-2} for A496 (values from Table 5 of Edge & Stewart 1991). For simultaneous fits, we required the temperature, column density, and abundance to vary jointly between each data set at a given radius while allowing the individual normalizations to vary independently as a result of variations in the response matrices.

Response matrices for BBXRT vary with the individual pixel and the off-axis angle of the source in each observation. The first occurs primarily as a result of differences in thickness of the gold layer on each pixel. The off-axis angle is important because higher energy photons are lost preferentially by the telescope vignetting. Appropriate response matrices were produced for each significant pixel and off-axis angle. We then fitted the spectrum from each pixel to determine the significance of variations in the response matrix of each pixel. Pixels with response curves differing by more than 10% across small bands ~100 eV wide were considered incompatible for summation. In general, the A and B matrices can not be co-added as a result of the differences in the thickness of the gold layer. The A matrices were discovered to introduce spectral differences of less than ~10%, well within the noise from photon statistics in a given spectrum. The B matrices behaved similarly with the exception that the B0 response matrix differed from other B pixel responses by more than 10%, so we did not add the B0 pixel to any other pixel. In the case where pixels could not be added, but for which it was desirable to add pixels based on radius and temperature, fits were done simultaneously using XSPEC. Finally, changes in the off-axis angle by a few arcminutes did not change the resulting fit. As a result, we constructed a response matrix for each pixel or pixel sum for A496 using an off-axis angle of 3′ instead of constructing response matrices at 2′ and 4′. For A262, response matrices of 7′ were used for the first and third observations, and matrices with an off-axis angle of 13′ were used for the second and fourth observations. We acknowledge that we have not eliminated small (<10%) systematic errors; however, the limited data set allows only gross systematic errors greater than 15% to be visible. We believe we have eliminated errors of that size or larger.

While BBXRT functioned over the range 0.3–10 keV, Weaver et al. (1995) determined that not all of the pixels were calibrated reliably over the entire range. Specifically, each pixel has a lower threshold channel below which its calibration is not reliable. Data in channels below the energy of these lowest reliable channels were ignored during the fitting process. This was done after the pixels were co-added channel by channel to preserve the energy-channel relationship. In addition, we ignored channels over 450 (corresponding to an energy of ~9–10 keV) for all fits as a result of the extremely low signal at high energies.

3.2. *Combining Pixels for Spectral Fitting*

3.2.1. *A496*

Three pairs of overlapping pixels (2A2/2B4; 4A3/4B1; 4A4/4B2) were omitted from subsequent analysis because the signal was very weak (Table 1). These pixels were the farthest from the cluster in each observation. Jahoda et al. (1992) fitted the BBXRT diffuse X-ray background with a broken power-law model with photon indices of 6.0 and 1.4, the break occurring at approximately 0.8 keV. Spectral fits of these outer pixels indicated that they were consistent with the Jahoda et al. (1992) diffuse background fits. The remaining pixels were combined as described in the section above. The resulting combinations were arrived at by always pairing overlapping pixels (e.g., A1 with B3), and by co-adding pixels having radial distances within 1.′0 of each other. The resulting combinations are shown in Table 2.

3.2.2. *A262*

In the case of A262, a large number of pixels were also omitted from subsequent analysis because of the weak signal resulting from the off-axis pointing (Table 1). The pixels omitted from each observation are as follows: (1) B0,

TABLE 2

SPECTRAL FIT RESULTS[a]

Pixel Number	Pixel Combinations[b]	Radius Range[c]	Low-Energy Cutoff[d]	kT (keV)	N_H (10^{22} cm^{-2})	Abundance	χ^2	Flux[e]
				A496				
1........	4A0 and 4B0	1.3–2.0	0.45	$2.84^{+0.50}_{-0.40}$	0.11 ± 0.05	$1.15^{+0.85}_{-0.55}$	1.22	3.7
2........	(2A0 + 2A4) and 2B0 and 2B2	2.6–3.6	0.53	3.29 ± 0.18	0.14 ± 0.02	0.49 ± 0.10	1.03	10.1
3........	4A2 and 4B4	4.0–4.9	0.50	$4.01^{+1.03}_{-0.66}$	$0.10^{+0.05}_{-0.04}$	$0.34^{+0.47}_{-0.34}$	1.02	4.9
4........	(2A3 + 4A1) and (2B1 + 4B3)	5.2–6.2	0.60	$3.80^{+0.55}_{-0.46}$	0.17 ± 0.04	$0.35^{+0.25}_{-0.15}$	0.97	3.8
5........	2A1 and 2B3	7.6	0.50	$4.07^{+0.90}_{-0.60}$	$0.13^{+0.06}_{-0.04}$	$0.67^{+0.50}_{-0.37}$	0.96	1.8
				A262				
1........	(1B1 + 3B1 + 3B4) and (1A3 + 3A0 + 3A2 + 3A3)	3.4–6.5	0.55	$2.14^{+0.40}_{-0.30}$	$0.15^{+0.03}_{-0.02}$	$0.51^{+0.25}_{-0.15}$	0.96	7.1
2........	(2A3 + 4A3) and (2B1 + 4B1)	6.4–6.9	0.55	$3.40^{+1.15}_{-0.75}$	$0.05^{+0.06}_{-0.04}$	$0.95^{+1.45}_{-0.60}$	0.95	3.1
3........	(1A0 + 1A2 + 3A1 + 3A4) and (1B4 + 3B2 + 3B3)	7.0–9.5	0.55	$3.15^{+0.95}_{-0.60}$	0.06 ± 0.05	$0.49^{+0.53}_{-0.30}$	0.60	3.1

[a] All error bars are 1 σ.

[b] For combining pixels, a " + " indicates co-adding, " and " indicates simultaneous fits.

[c] " Radius range " is the range in the radial distances in arcminutes of the center of the pixels used in each combination.

[d] The low-energy cutoff was determined after co-adding the spectra channel by channel. The cutoff is the highest energy for which any member pixel has an unreliable calibration.

[e] Model flux in units of 10^{-11} ergs cm^{-2} s^{-1} for the 1–8 keV band with the absorption set to zero.

A1/B3, and A4/B2; (2) A0/B0, A1/B3, A2/B4, and A4/B2; (3) B0; (4) A0/B0, A1/B3, A2/B4, and A4/B2. In each case, pairs of overlapping pixels were omitted, except for B0 in pointing 3. Model fits to each of these pixels individually were consistent with no signal.

Simultaneous fits of three pixels, appropriately co-added, were consistent with the diffuse background of Jahoda et al. (1992). Over half of the pixels were subsequently omitted from our analysis. To boost the signal for the spectral fit, we added as many of the remaining pixels together as was consistent with the criteria outlined in § 3.1. Only two combinations of pixels could be co-added: pixels from pointings 1 and 3 (off-axis angles of 4′ and 9′, respectively) and pixels from pointings 2 and 4 (off-axis angles of 13′ each). The pixel combinations resulted in three co-added pixels: (1) pixels from the first and third observation at small radial distances; (2) pixels from the second and fourth observation; (3) pixels from the first and third observation at large radial distances. In each case, pixels with compatible responses were co-added and then the A and B telescope data were simultaneously fitted. Pixel combinations used for spectral fitting are summarized in Table 2.

4. SPECTRAL FIT RESULTS

4.1. *A496*

Figure 2 shows an observed spectrum and its fitted model for A496 pixel 2A0 + 2A4 (note that the spectrum is plotted on a log flux scale, while the residuals are plotted on a linear flux scale). The best-fit model is a simultaneous fit of this pixel and pixels 2B0 and 2B2 (fit 2 in Table 2) using a Raymond-Smith (1977) thermal bremsstrahlung component and a Galactic absorption model (Morrison & McCammon 1983). Once the fit was complete, pixels 2B0 and 2B2 were removed from the display for clarity. Table 2 presents the best-fit model results for all pixel combinations. Confidence contours of temperature versus the column density are shown in Figure 3 for the same pixel as displayed in Figure 2. The contours represent equal χ^2 increments above the minimum χ^2 (marked with a +). From innermost to outermost, the contours are the 1 σ, 90%, and 99% errors for two parameters of interest.

Figure 4 is a plot of the fitted spectral parameters against the projected radial distance from the center of the cluster. Vertical error bars are the 1 σ errors in the parameter. Horizontal error bars represent the physical size of the pixels used in each spectral fit. Figure 4*a* shows that the cluster temperature varies from 2.9 keV to 4.0 keV over the range of radial distances. To confirm that we were detecting the cluster cooling flow, we verified the following: the observations were all of the correct source; the off-axis angles were correct and the response matrices were appropriate for the off-axis angle; the overlay of the BBXRT pixels onto a X-ray image of the cluster gave an accurate picture of the pixel that was receiving the bulk of the data; and low-energy contamination from atmospheric oxygen and nitrogen near 0.5 keV were not affecting the spectral fit. David et al. (1993) list values of kT for the intracluster gas, obtained by fitting the *Einstein* MPC spectra, plus data from *EXOSAT* and *Ginga*. The David et al. (1993) temperature for A496 is indicated by a solid line in Figure 4*a*. If we adopt this temperature as the "cluster temperature," then the value of χ^2 is 16.1 for the complete data set, with the largest contribution coming from the innermost pixel. If we *fit* a constant temperature to the individual temperatures, the reduced χ^2 value is 2.8 for a fitted temperature of 3.3 keV, which is outside of the 1 σ error range for the cluster temperature listed in David et al. (1993). We acknowledge that the temperature gradient detection is statistically marginal (significant at ~90%), but we conclude the temperature variation is very probably a real detection in spite of the limited spatial resolution of the BBXRT pixels.

The best-fit values of the absorption show that it is relatively uniform across the cluster at the spatial resolution of BBXRT. Figure 4*b* shows the column density values, with 1 σ errors, for each of our pixels. The mean value is $0.12^{+0.06}_{-0.07}$ (90% error range) in units of 10^{22} cm^{-2}. The 90% range does not include the Galactic value of 0.045 (*solid line*), so there is marginal evidence for higher absorption at the cluster center. Pixel combination number 2 is inconsistent with the Galactic column density at the 99% level, suggesting the column density varies across the face of the

1996ApJ...468...86M

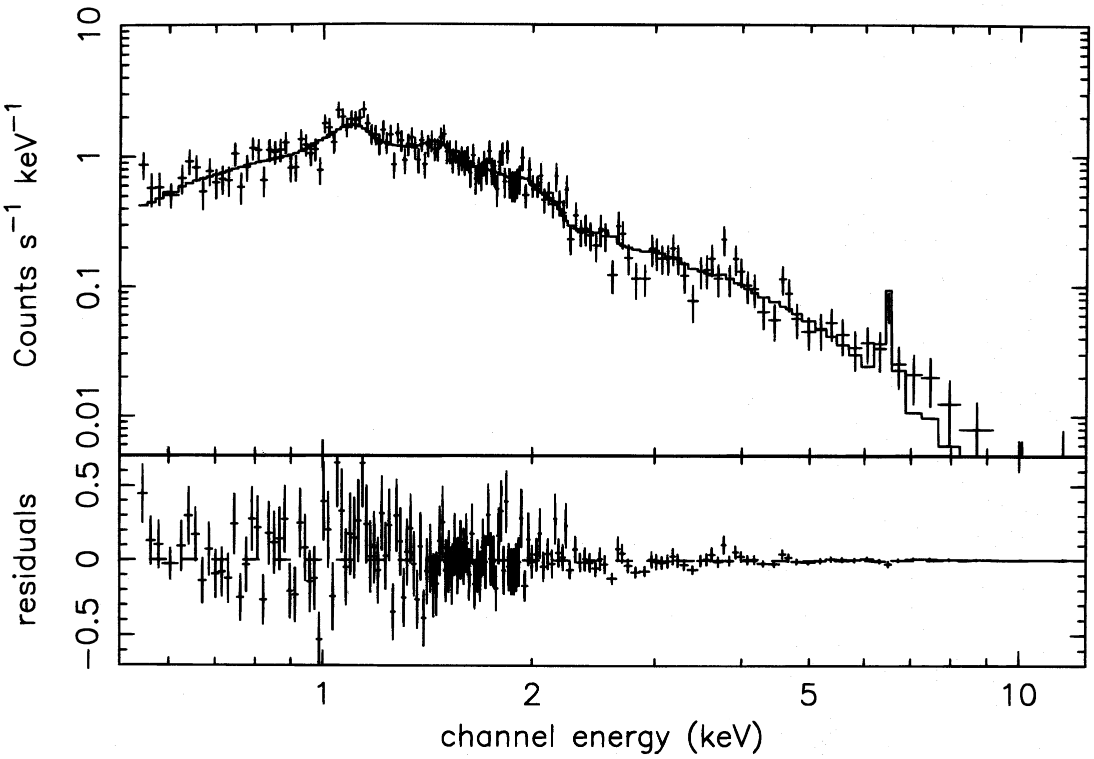

FIG. 2.—BBXRT spectrum (*log flux scale*) and residuals (*linear scale*) of the fit to A496 pixel combination number 2. We show only the 2A0 spectrum for clarity, and the data are binned for display. Data points have 1 σ error bars. The simultaneous fit for the two combinations yielded the same results, differing only in the normalizations.

cluster. A higher spatial resolution observation will be necessary to weaken or to strengthen the marginal evidence from the BBXRT pixels.

The best-fit values of the abundance for each pixel are shown in Figure 4*c*. Again, 1 σ error bars are shown. The outer four pixels are consistent with a constant cluster abundance of ∼0.49. The innermost pixel, while consistent with a cluster abundance of ∼0.49 at the 2 σ level, suggests that the cluster's abundance may rise toward the center. We stress again that the evidence is marginal, but worthy of confirmation with *ASCA* or future missions.

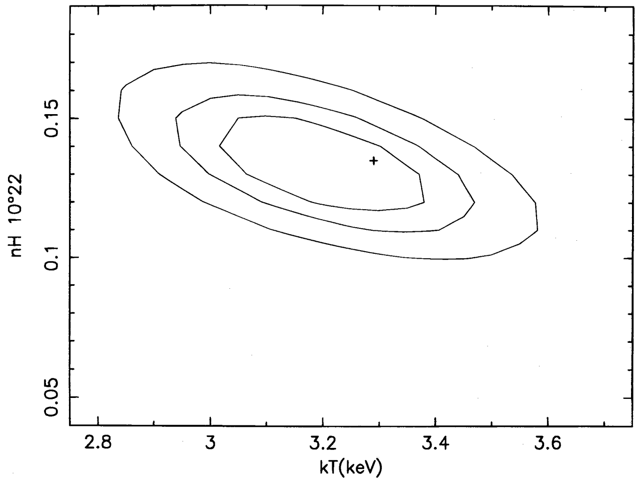

FIG. 3.—Confidence contours for A496 gas temperature vs. the column density for pixel combination number 2. The contour values are $\Delta\chi^2 = 2.71, 4.61$, and 9.71.

As stated above, we expect to see emission lines in the spectrum of the cluster gas, with the iron K line in the 6.5–6.9 keV region as the strongest emitter. We were able to fit the line only in one of the A496 pixel combinations since the line flux varies as a function of radial distance in the cluster. We added a Gaussian component to the best-fit continuum spectral model and permitted the line energy, physical width, and the line flux to vary.

Figure 5 gives an expanded view of the region around iron K for the pixels 2A0 + 2A4 (pixel combination number 2). The data are binned for display purposes only. The fit is consistent with a zero width line at $6.46^{+0.05}_{-0.04}$ keV with an equivalent width of 597 eV. This line is at 6.66 keV in the rest frame of the cluster, an energy corresponding to Fe xxv. The 1 σ error values were obtained by stepping the line energy in energy until χ^2 changed by 2.7. The resulting energy range was 6.42–6.51 keV in the detector rest frame. We can also invert this result: if we assume the line is Fe xxv, then the cluster's X-ray redshift is $z \sim 0.03$, consistent with the optically measured redshift of individual galaxies in the cluster. Again, better quality data would measure the redshift more precisely.

We tested for the presence of Fe Kα 6.4 and Fe xxvi 6.9 keV lines by fixing the line energy at 6.20 and 6.69 keV, the redshifted energies of these lines. No fit was attempted; instead, the line normalizations were raised until $\Delta\chi^2$ increased by +2.71, the 90% confidence level for one parameter of interest. The equivalent widths were then calculated. The values are ∼2 keV, unrestrictive because of the low signal-to-noise of the continuum at the line positions.

4.2. *A262*

Figures 6 and 7 show an observed spectrum with fitted model and confidence contours for one A262 pixel, as was

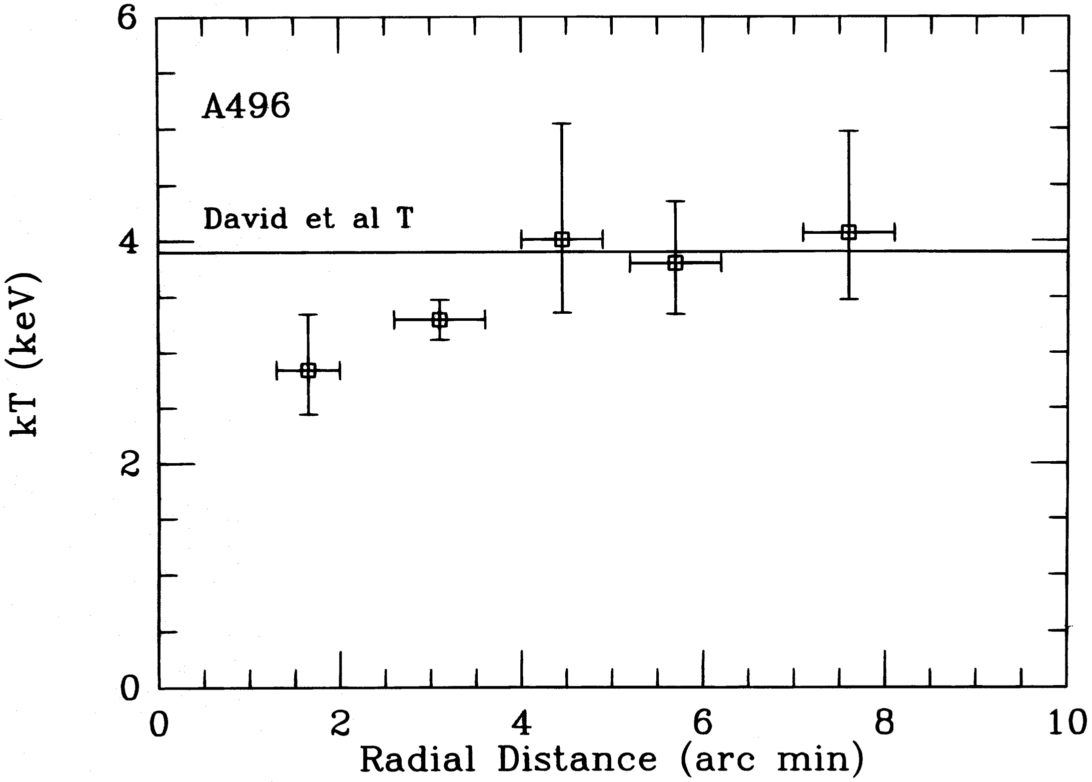

FIG. 4*a*

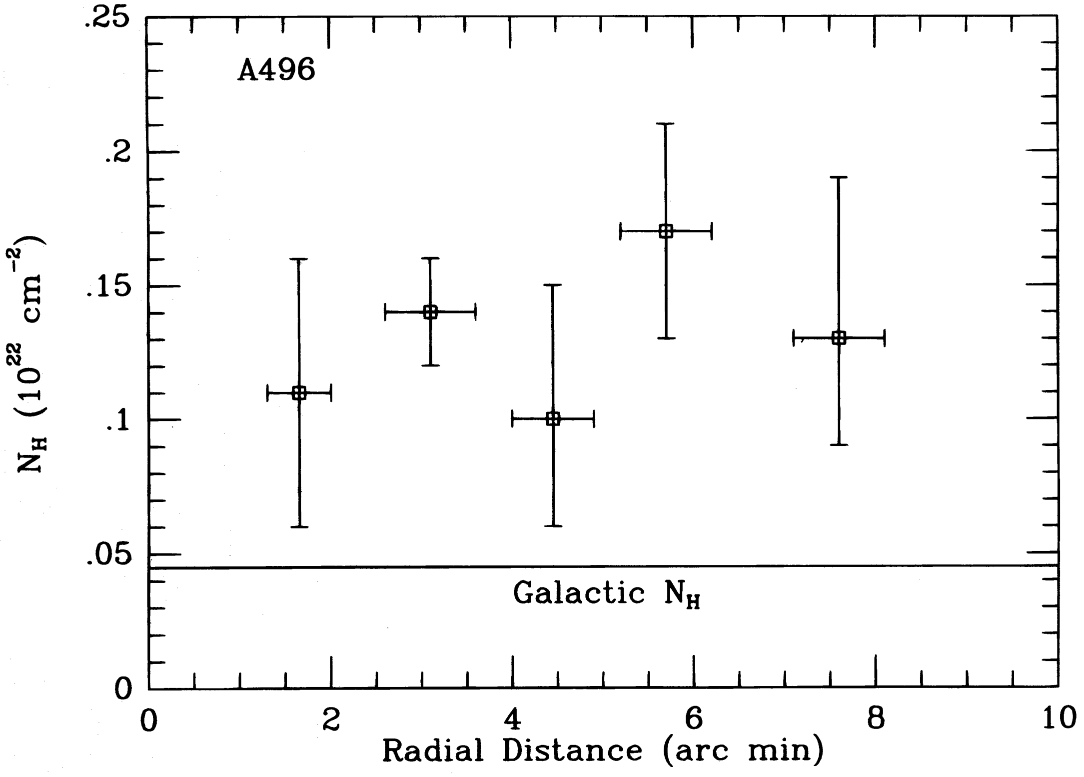

FIG. 4*b*

FIG. 4.—A496 fitted spectral parameters plotted as a function of cluster radius. Vertical error bars represent 1 σ errors. Horizontal bars represent the range of the combined pixel. (*a*) Gas temperature; (*b*) column density; (*c*) abundance.

done for A496 above. Best-fit models for the innermost pixel combination were found in the same way as for A496 and the fit results also appear in Table 2. For the middle and outer pixel combinations, the fits were not convergently stable if the column density and the abundance were permitted to vary simultaneously. We therefore fixed the column density at the literature value and varied the abundance. We then froze the abundance at the best-fit value

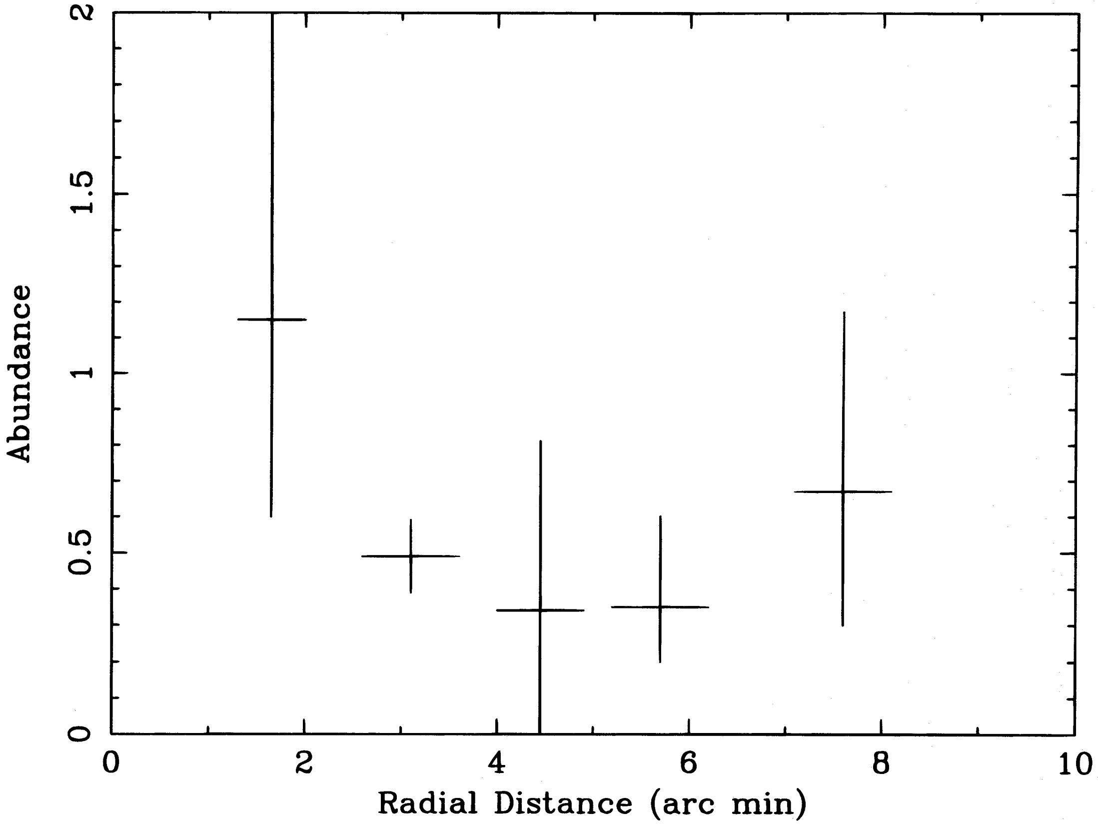

FIG. 4*c*

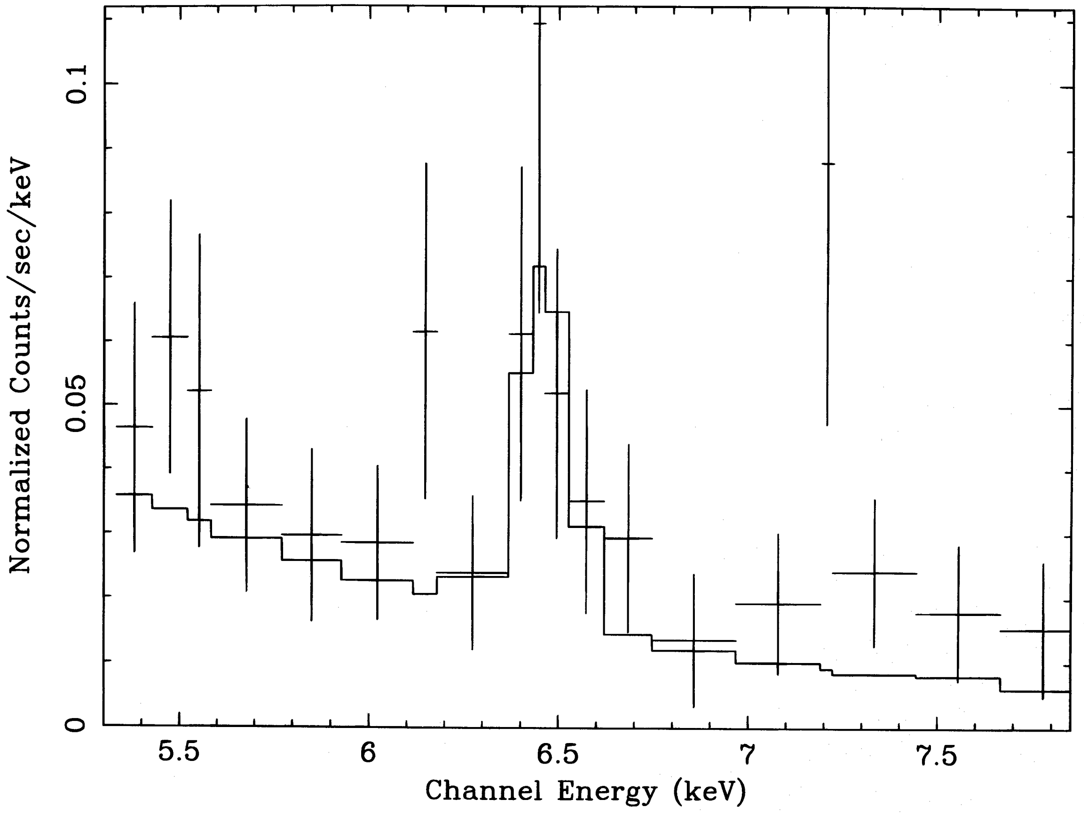

FIG. 5.—Expanded view of the iron K line region in A496 on a linear energy scale. Data are binned for display only.

1996ApJ...468...86M

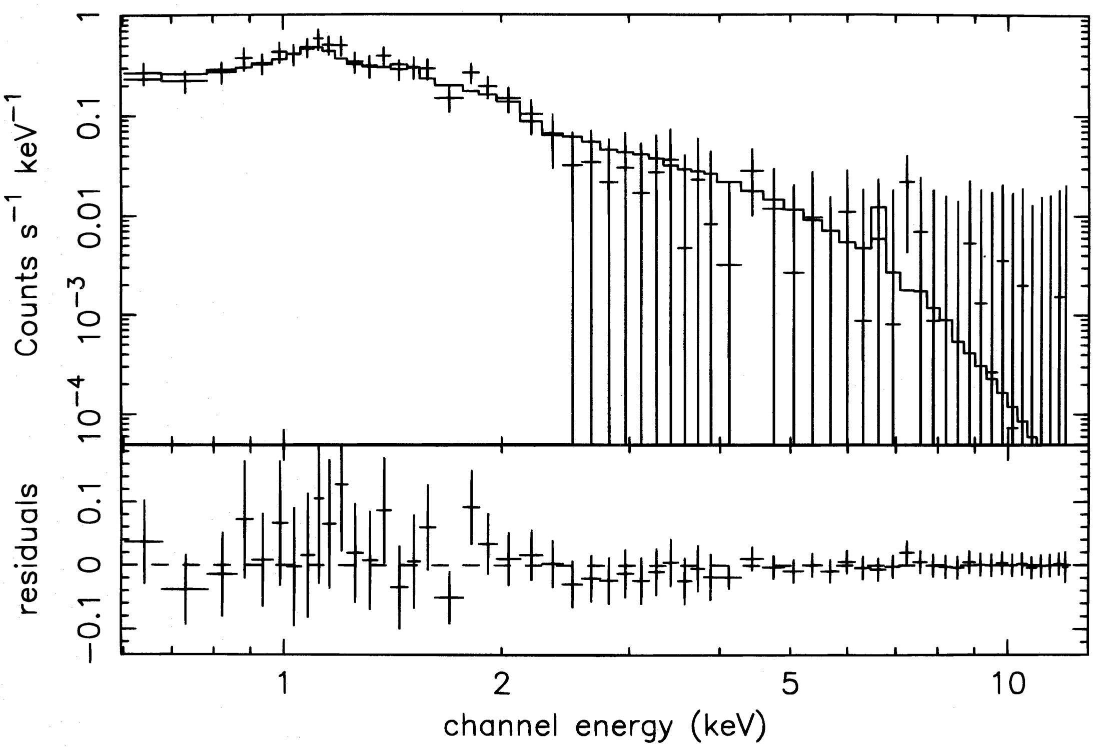

FIG. 6.—BBXRT spectrum (*log flux scale*) and the residuals (*linear scale*) of the fit to A262 pixel combination number 2. We show only the 2A3+4A3 spectrum for clarity, and the data are binned for display. The figure is plotted in the same manner as in Fig. 2.

and varied the column density. In this manner, after another iteration, we reached a solution in which neither parameter varied from the best-fit value by more than ~10%. The temperature throughout this process did not vary by more than ~10% either.

Figure 8 is a plot of the fitted spectral parameters as a function of radial distance. Figure 8*a* shows the temperature, which varied from 2.1 to 3.4 keV. In this case, the error bars are sufficiently large that no temperature gradient has been detected. The fitted temperatures are consistent with the intracluster gas temperature of 2.4 keV listed in David et al. (1993). It is important to note, however, that these results are primarily relevant to the outer regions of the cluster since all of the observations occurred at off-axis angles greater than 4′. None of the BBXRT pointings sampled the cluster core as well as was done with the A496 pointings. Figures 8*b* and 8*c* show the column density and abundance parameters, respectively. The outer two pixel combinations are consistent with the literature value; the innermost pixel is inconsistent with the literature value at the 90% level, but consistent at 99%. The abundances have a mean value of 0.51 with large error bars.

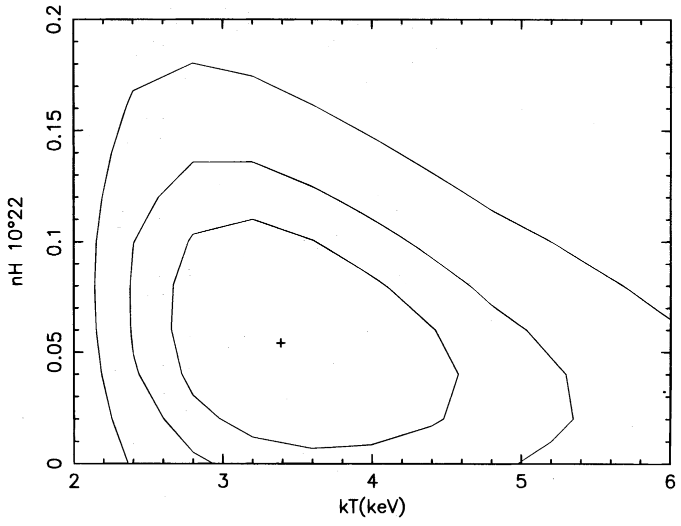

FIG. 7.—Confidence contours for A262 gas temperature vs. the column density for pixel combination number 2. The contour values are as in Fig. 3.

No iron line is visible in the data for A262. We determined an upper limit in the same manner as described above for the A496 6.4 and 6.9 keV lines. For A262, we also tested for the presence of the Fe XXV 6.8 keV line. For A262, the 3 σ upper limit on the presence of an iron line is unrestrictive at ~2 keV.

5. DISCUSSION

The results presented above appear quite robust in spite of the limited signal-to-noise ratio in the data and the limited spatial resolution of the BBXRT pixels.

We believe a gradient in the temperature of the fitted spectra is visible (Fig. 4*a*). In Figure 9 we compare the derived temperatures from the BBXRT data with the deprojected temperature profile from *Einstein* IPC and HRI data (Edge, Stewart, & Fabian 1992). The BBXRT values, while providing rather poor spatial resolution on a per pixel basis, do provide some resolution of the cluster cooling flow as a result of the off-axis pointings. The overall shape of the temperature profile is completely consistent with the Edge et al. (1992) results.

The mass within the cooling flow may be estimated approximately by making the usual assumption of hydro-

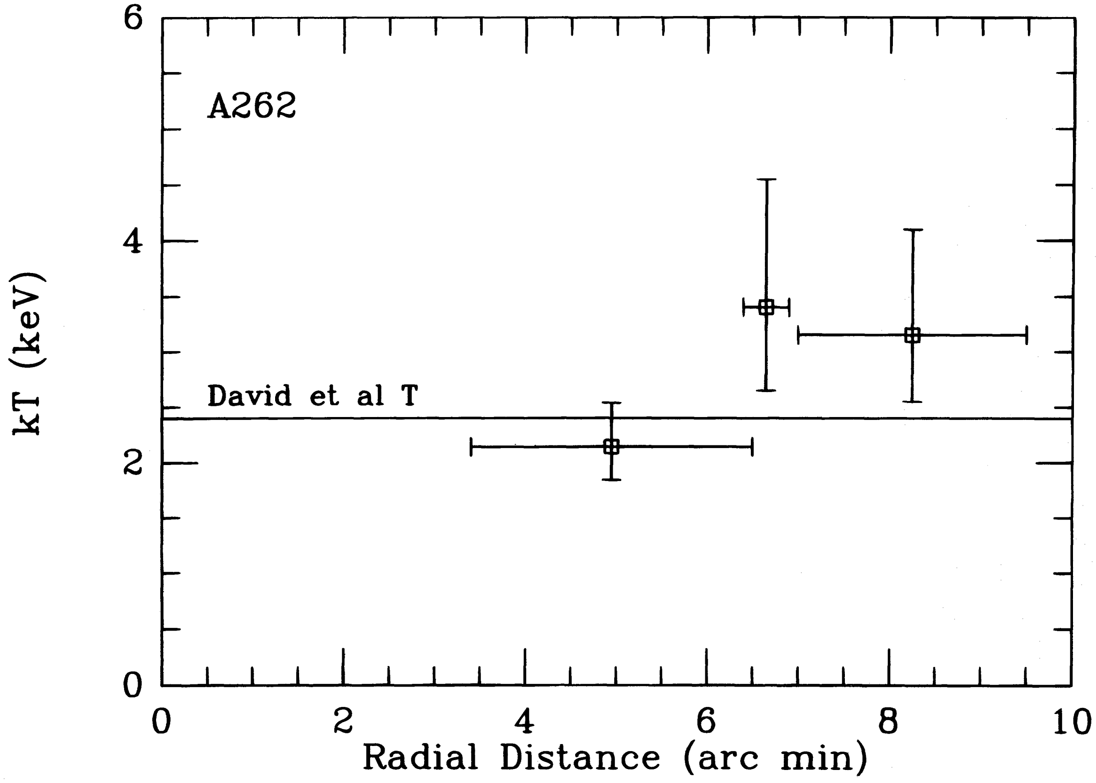

FIG. 8*a*

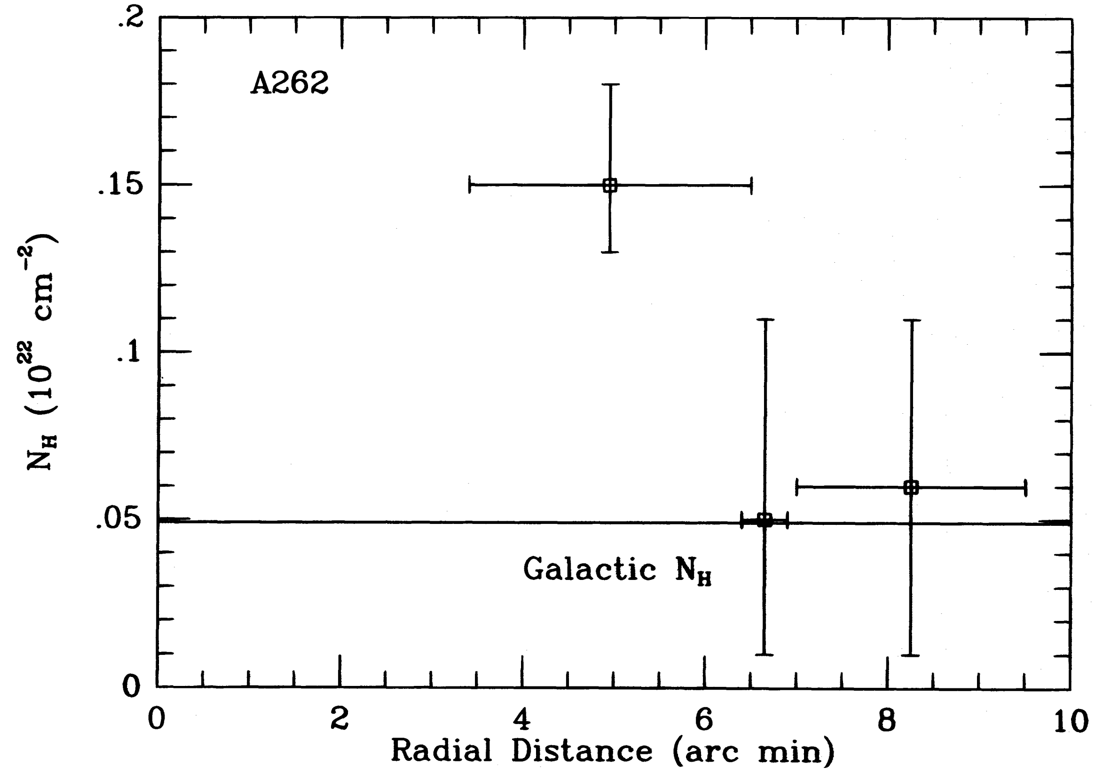

FIG. 8*b*

FIG. 8.—A262 fitted spectral parameters plotted as a function of cluster radius. Error bars are as in Fig. 4. (*a*) Gas temperature; (*b*) column density; and (*c*) abundance.

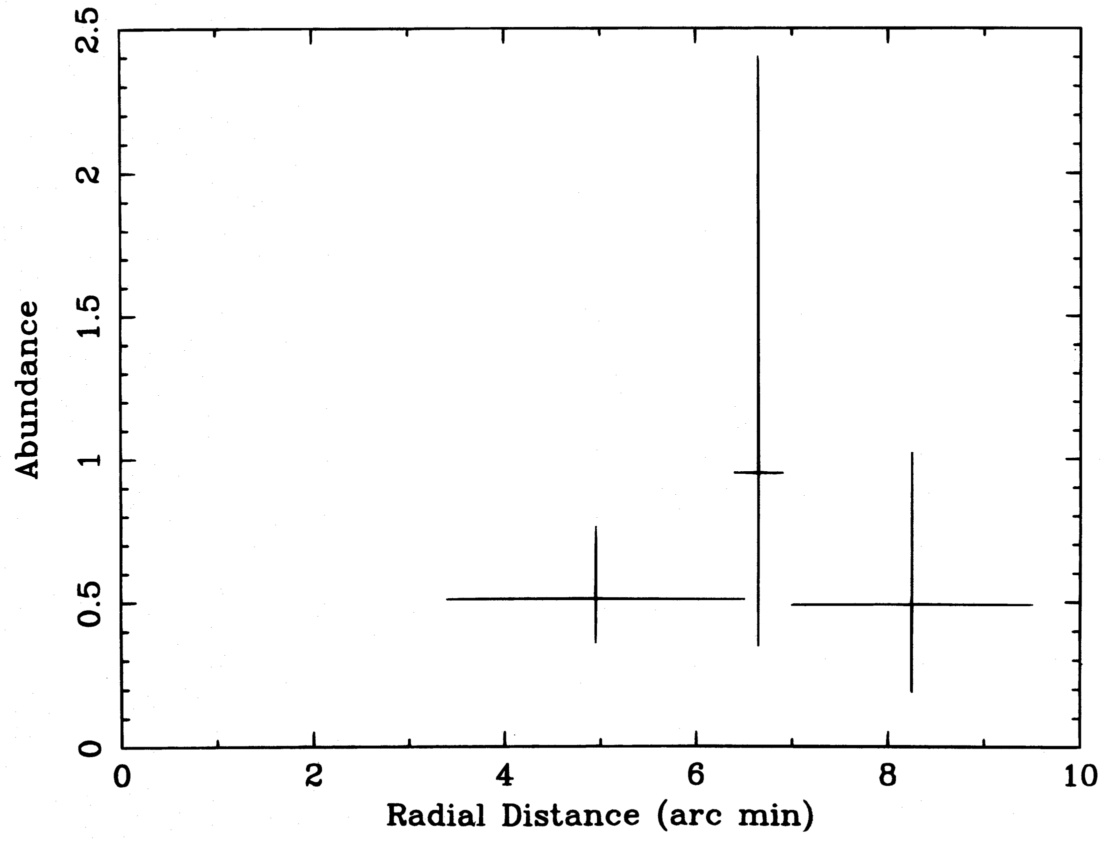

FIG. 8*c*

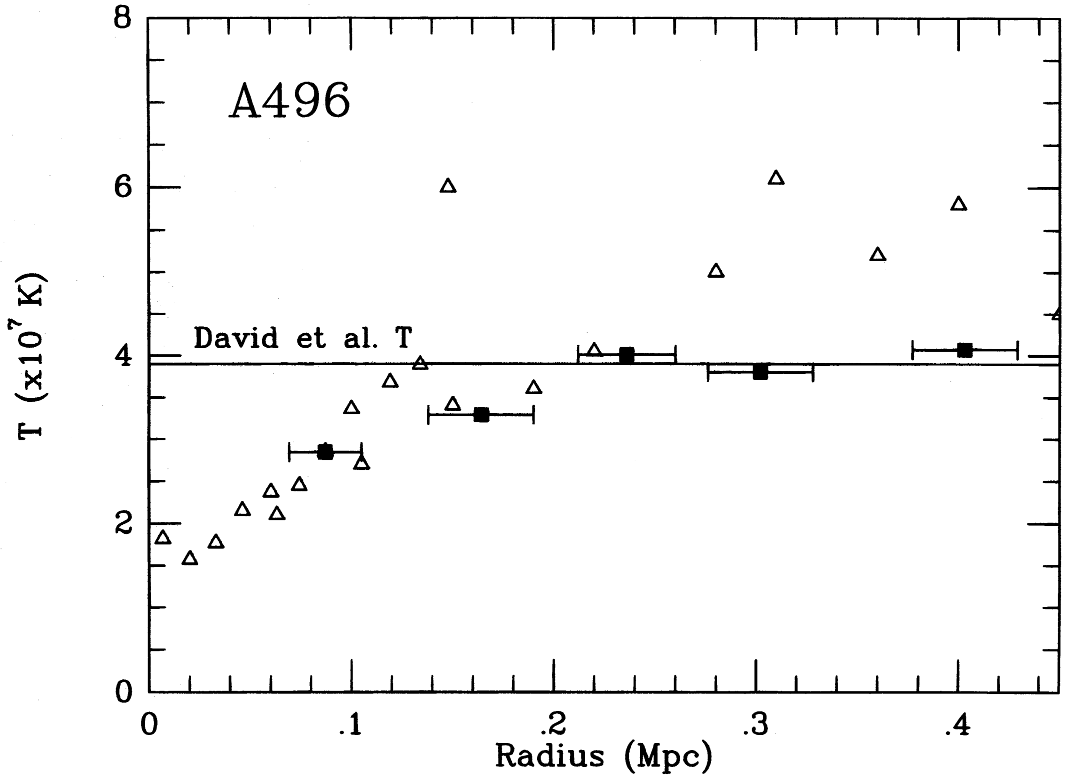

FIG. 9.—BBXRT temperature profile (*filled squares*), without vertical error bars, in comparison with the temperature profile (*triangles*) from Edge et al. (1992). No error bars have been included on the Edge et al. (1992) points, which originally were a mix of measurements from IPC and HRI data (roughly, values within 0.1 Mpc are HRI values, while values outside of 0.1 Mpc are IPC measurements).

static equilibrium, namely,

$$M(<r) = -\left(\frac{kT_g}{G\mu m_{\rm H}}\right)\left(\frac{d\log\rho_g}{d\log r} + \frac{d\log T_g}{d\log r}\right)r\,,$$

where the variables have their usual meanings. The second term in the parentheses comes from fitting the profile in Figure 4. We fitted a simple linear model to the Figure 4 data because of the limited number of temperature samples. The slope of the fit was 0.16 ± 0.14 (90% error); adding a higher order term did not alter the fit from linear. The value of the first term comes from fitting the standard King model to the *ROSAT* Position Sensitive Proportional Counter (PSPC) data extracted from the archive (principal investigator, G. Kriss). The radial profile was constructed by extracting the counts in 8″ annuli from the center outward to 380″ with subsequent fitting of the profile. We used the standard King model, $S = S_0[1 + (R/R_c)^2]^{-n}$. The fitted value of the exponent n $(3\beta - \frac{1}{2})$ was 0.787 ± 0.011, giving a value for $d \log \rho / d \log r = -1.28 \pm 0.01$. Inserting all of these values yields $M(<r) \sim (7.4 \pm 1.0) \times 10^{13}$ $M_\odot$. The preliminary value from the *ASCA* data is $M(<Gr) \sim (2.5 \pm 0.1) \times 10^{14}$ $M_\odot$ for $r < 1$ Mpc (Mushotzky 1994). Scaling that value to 0.3 Mpc yields a mass $\sim 7.5 \times 10^{13}$ $M_\odot$, so the BBXRT value agrees, to within a few percent, with the *ASCA* value. The error range is large, however, so the BBXRT measurement is not precise.

White et al. (1994) show, with a joint spectral fit on data from the *Einstein* SSS and from the *Ginga* LAC, that a two-temperature Raymond-Smith model gave a best fit with high- and low-temperature components. We attempted to duplicate this fit, but were unable to do so. We believe the two-temperature fit stems from the relatively large fields of view of the SSS and the LAC.

White et al. (1994) did find the column density was elevated for A496. Our A496 data are marginally consistent with a constant, but elevated, absorption column density across the face of the cluster, and show marginal evidence for variations. The BBXRT short pointing may have sufficiently reduced the detected signal that photon statistics are masking a gradient. The *ROSAT* PSPC data show column density variations, in particular, excess absorption (Cannon & Ponman 1995). Within the formal errors from the spectral fitting, we also have no evidence for abundance variations, although marginal evidence exists for enhanced abundances in the cluster core. A496 shows an iron line, consistent with Fe XXV, but no other lines of Fe are visible in any of the likely locations.

The A262 data are unfortunately of limited value. There is no evidence for any abundance variations, nor of column density variations. The temperature profile is relatively flat, nearly consistent with no cooling flow, but we again note that the BBXRT pointings were all obtained outside the cluster core. Edge et al. (1992) list a cooling flow of ~67 $M_\odot$ (90 percentile) for A262. We did not calculate a mass for the cluster, since we judged the error bars to be sufficiently large that our value would be easily consistent with previous values. No evidence exists for an iron line with an upper limit of ~1 keV.

In summary, the BBXRT data reveal evidence for a temperature and an abundance gradient and enhanced absorption across the face of A496. The evidence for enhanced absorption in A262 is limited to one pixel, and no evidence is available for gradients in temperature or abundance, but the BBXRT pointings were sufficiently off-axis that the cluster core was not observed. BBXRT has demonstrated, however, the power of high spectral resolution combined with spatial resolution. We eagerly await a high–spatial resolution, high–spectral resolution instrument so that we can probe these clusters in greater detail.

We thank Mike Loewenstein for useful conversations and the anonymous referee for improvements to the manuscript.

REFERENCES

Cannon, D., & Ponman, T. 1995, in Proc. Maryland October Astrophysics Conference, Dark Matter, ed. S. Holt & C. Bennett (New York: AIP), 264

David, L., Slyz, A., Jones, C., Forman, W., Vrtilek, S., & Arnaud, K. 1993, ApJ, 412, 479

Edge, A., & Stewart, G. 1991, MNRAS, 252, 414

Edge, A., Stewart, G., & Fabian, A. 1992, MNRAS, 258, 177

Edge, A., Stewart, G., Fabian, A., & Arnaud, K. 1990, MNRAS, 245, 559

Fabian, A. 1994, ARA&A, 32, 277

Forman, W., Jones, C., Cominsky, L., Julien, P., Murray, S., Peters, G., Tananbaum, H., & Giacconi, R. 1978, ApJS, 38, 357

Jahoda, K., et al. 1992, in The X-Ray Background, ed. X. Barcons & A. Fabian (Cambridge: Cambridge Univ. Press), 240

Mitchell, R., Culhane, J., Davison, P., & Ives, J. 1976, MNRAS, 189, 329

Morrison, A., & McCammon, D. 1983, ApJ, 270, 119

Mushotzky, R. 1994, Clusters of Galaxies, ed. F. Durret, A. Mazure, & J. Tran Thanh Van, (Gif-Sur-Yvette Cedex: Editions Frontières), 167

Nulsen, P., Stewart, G., Fabian, A., Mushotzky, R., Holt, S., Ku, W., & Malin, D. 1982, MNRAS, 199, 1089

Raymond, J. C., & Smith, B. W. 1977, ApJS, 35, 419

Sarazin, C. 1986, Rev. Mod. Phys., 58, 1

———. 1988, X-Ray Emission from Clusters of Galaxies (Cambridge: Cambridge Univ. Press)

Serlemitsos, P., et al. 1992, in Frontiers of X-Ray Astronomy, ed. Y. Tanaka & K. Koyama (Tokyo: Universal Academy), 221

Serlemitsos, P., Smith, B., Boldt, E., Holt, S., & Swank, J. 1977, ApJ, 211, L63

Stewart, G., Fabian, A., Jones, C., & Forman, W. 1984, ApJ, 285, 1

Weaver, K., et al. 1995, ApJS, 96, 303

White, D., Fabian, A., Johnstone, R., Mushotzky, R., & Arnaud, K. 1991, MNRAS, 252, 72

White, R. E., III, Day, C. S. R., Hatsukade, I., & Hughes, J. P. 1994, ApJ, 433, 583